# Point defects and their reactions in $e^-$-irradiated GaAs investigated by x-ray-diffraction methods

A. Pillukat,* K. Karsten, and P. Ehrhart
*Institut für Festkörperforschung des Forschungszentrums Jülich, D-52425 Jülich, Germany*
(Received 15 March 1995; revised manuscript received 3 October 1995)

Semi-insulating as well as *n*-type and *p*-type GaAs wafers have been irradiated at 4.5 K with 3-MeV electrons up to doses between 0.6 and $3.6\times10^{19}$ $e^-/cm^2$. Without intermediate warming the irradiated samples were investigated by measurements of the change of the lattice parameter and of the diffuse scattering intensity close to different Bragg reflections. These measurements give direct access to the structure of interstitial atoms in GaAs. Two types of Frenkel defects can be distinguished due to their different annealing at room temperature and around 500 K, respectively. The details of the distribution of the scattering intensity indicate the dominating role of close Frenkel pairs with a typical distance of $\approx$10 Å between vacancies and interstitial atoms for the structure of the low-temperature defects. The unusually large strain field or the relaxation volume of $\approx$2.0 atomic volumes indicates in addition that these defects arise from double displacements. The Frenkel pairs that anneal around 500 K are characterized by a much smaller relaxation volume of $\approx$1 atomic volume. Defect introduction rates of $\approx1$ $cm^{-1}$ have been determined and show that total defect densities of $3\times10^{19}$ $cm^{-3}$ can be achieved without indication of saturation or defect clustering. The defect reactions during irradiation as well as during thermal annealing up to 800 K are discussed with special emphasis on the trapping and detrapping of mobile interstitials at other intrinsic defects and the suppression of the formation of dislocation loops. There is no relevant difference observed between the differently doped samples after these high dose irradiations.

## I. INTRODUCTION

Point defects and their complexes determine the electrical properties of semiconductors and have been investigated in detail for many years. Nevertheless, there is not yet a consistent picture of the properties of even the simplest intrinsic defects (i.e., vacancies, interstitial atoms, and antisites) in III-V compounds and there is a long standing discussion on the structure of the $EL2$ defect in GaAs,[1–4] that yields the electrical compensation of undoped semi-insulating GaAs. Detailed arguments have been presented for the attribution of $EL2$ to the isolated As antisite, $As_{Ga}$,[4,5] as well as to a complex of $As_{Ga}$, with an arsenic interstitial atom.[6,7] For a better understanding of such complexes, the properties of interstitial atoms would be very helpful. However, there is at present no direct information as, in contrast to some theoretical expectations, no energy level due to interstitial atoms could be identified within the band gap. Therefore, interstitial atoms are not accessible for most experimental methods. Hence, we decided to use x-ray-diffraction (XRD) techniques, i.e., measurements of the change of the lattice parameter in combination with measurements of the Huang diffuse scattering (HDS). These techniques detect all defects, independent of their electronic properties, as long as they induce atomic displacement fields. The rather high defect concentrations that are necessary for these techniques can be produced by electron irradiation in the form of Frenkel pairs (FP), i.e., pairs of interstitial atoms and vacancies.

The electrical properties of these irradiation defects have been investigated in detail by deep level transient spectroscopy (DLTS) and these results have been reviewed recently.[7,2] The DLTS spectra are dominated by levels that are stable up to an annealing stage around 500 K [stage III, (Ref. 8)]. These DLTS levels are produced with a threshold energy $E_d\approx10$ eV and are attributed to FP's on the As sublattice, due to the anisotropy of their introduction rates.[7] As there were no other significant DLTS levels, FP's on the Ga sublattice were assumed to be unstable. In contrast to DLTS, the investigation of the electrical conductivity of *n*-type GaAs revealed major defect annealing below room temperature: the annealing stages I and II.[8] Major annealing below room temperature (RT) was also observed for the radiation induced changes of the thermal conductivity[9] and of the length changes.[10] Positron annihilation spectroscopy (PAS) showed that Ga vacancies anneal within these low temperature annealing stages[11–13] and, therefore, it seems that FP's on the two sublattices might react quite independently. A basic problem arises, however, for this simple picture, due to the observation that the ''Ga-FP's'' need about twice the threshold energy $T_D\approx$ 20 eV as arsenic FP's. This high threshold energy would allow also for double displacements and suggests more complex defect patterns. Hence, further investigations of the detailed defect structures seem necessary.

In order to arrive at the most simple defect pattern, our irradiations were performed at 4.5 K. As GaAs becomes semi-insulating (s.i.) after high dose irradiations, we started with s.i. GaAs in order to avoid larger shifts of the Fermi level during irradiation and annealing. In spite of possible ionization induced defect migrations that are generally discussed for semiconductors,[14,15] preliminary experiments showed that high concentrations of FP's could be frozen in (Refs. 16–18) by these irradiations. Hence, more detailed investigations were performed with s.i., as well as *n*-type ($2\times10^{17}$ Te $cm^{-3}$) and *p*-type ($3\times10^{18}$ Zn $cm^{-3}$) GaAs wafers. As we used rather high irradiation doses ($\phi t=6\times10^{18}-3\times10^{19}$ 3-MeV electrons/$cm^2$), all these samples were ''semi-insulating'' after irradiation, too. Nev-

 

ertheless, we would expect larger differences in the defect arrangement if these doping atoms would act as nucleation centers for larger defect agglomerates.

In the following section, we offer comments on the theory of the diffuse scattering and Sec. III summarizes the experimental details. The results of the XRD investigations are presented in Sec. IV and discussed in Sec. V.

## II. THEORETICAL BACKGROUND OF THE DIFFUSE SCATTERING TECHNIQUE

The theory of the diffuse scattering from point defects in crystals is well documented[19] and we have recently discussed the scattering from Frenkel defects in InP.[20] We repeat here only some definitions and refer to Ref. 20 for details. The Huang diffuse scattering is observed at small distances **q** of the scattering vector **k** from the corresponding reciprocal lattice vector **G**. The scattering cross section $S_H$ can be separated into a symmetric part $S_H^{\mathrm{sym}}$ which is determined by the long range displacement field of the defect, **s**, and an antisymmetric second order term $S_H^{\mathrm{asy}}$, which yields additional information on the closer vicinity. For a random distribution of defects, $S_H^{\mathrm{sym}}$ is determined by the product of the defect concentration $c$ and a quadratic expressions in the components of the dipole force tensor **P**. For cubic crystals, three independent quantities can be defined: $\pi^{(1)}=1/3\,\mathrm{Tr}\mathbf{P}^2$ and $\pi^{(2)}$, $\pi^{(3)}$ which characterize the defect symmetry [Eqs. (6), (7) of Ref. 20]. In combination with measurements of the lattice parameter $\Delta a/a$, the concentration $c$ and Tr**P** or $V^{\mathrm{rel}}=\mathrm{Tr}P/3B$ ($B$=bulk modulus) can be separated [Eq. (8), Ref. 20]. These interpretations are straightforward if there is only one type of defect; if there are, however, several defects present, the experiments yield ''average values.'' As we will consider Frenkel pairs, different contributions of interstitial atoms and vacancies $V_i^{\mathrm{rel}}$, $V_v^{\mathrm{rel}}$ must be considered in the following.

This approach will be modified if the basic assumption of a random distribution of defects is no longer valid and deviations from the characteristic $1/q^2$ behavior of $S_H$ [Eq. 6 of Ref. 20] are expected.[21] For the simple model of the formation of dense clusters by the agglomeration of point defects, the characteristic increase of the HDS can be quantitatively understood. A close FP presents a special defect correlation (or defect agglomerate) as it combines defects with displacement fields of opposite signs that are separated by a certain distance $R_{\mathrm{FP}}$. The scattering of such displacement fields has first been considered in order to simulate the scattering from defect agglomerates in $n$-irradiated GaAs (Ref. 22) and we have recently performed detailed calculations for FP's in InP,[20,23] using a linear superposition of elastically isotropic displacement fields around the vacancy and the interstitial atom. Some characteristic changes, as compared to a random distribution of defects, are observed: (i) We observe a decrease of the HDS at small values of $q$, which corresponds to the cancellation of the displacement fields at large distances from the FP:

$$S_H(q\rightarrow 0)\sim c(V_i^{\mathrm{rel}}+V_v^{\mathrm{rel}})^2, \tag{1}$$

where $c=c_i=c_v=c_{\mathrm{FP}}$. Due to the exact cancellation in the case of InP, the intensity even approaches zero for this special case. (ii) At larger values of $q$ we observe a higher intensity than for a random distribution of the defects. This increase is due to the large displacements between the FP that approach the value of the sum of the two fields. Hence, we expect for values of $q$ that reflect these small distances,

$$S_H(q\geqslant q_m)\sim c(V_i^{\mathrm{rel}}-V_v^{\mathrm{rel}})^2, \tag{2}$$

where $q_m\approx 1/R_{\mathrm{FP}}$. Averaging the experimental results over a limited region of $q$ around $q_m$ yields an average of Eqs. (1) and (2) and hence also a reasonable approximation of Eq. (8a) of Ref. 20. We can therefore combine Eq. (8) of Ref. 20 and Eq. (1) and can determine the three unknown parameters $c$, $V_i^{\mathrm{rel}}$, $V_v^{\mathrm{rel}}$, as long as there are only close FP's of one type. (iii) The calculations for this simple model show that the intensity distribution around a special reflection depends on the angle between **q** and $\mathbf{R}_{\mathrm{FP}}$ and yields, therefore, the symmetry of the defect pair and not that of the individual defects that were assumed to be isotropic. (iv) The exact positions of the defects additionally influence the asymmetry of $S$. Especially changes of the sign of $S^{\mathrm{asy}}$ can be observed if the center of the defects is different from highly symmetric lattice sites, because under these conditions, there is an additional phase factor between the center of the fields and the lattice sites.

## III. EXPERIMENTAL METHODS

### A. Samples and irradiations

Samples with a typical size of $5\times 15$ mm$^2$ were prepared from semi-insulating, $n$-type ($2\times 10^{17}$ Te cm$^{-3}$), and $p$-type ($3\times 10^{18}$ Zn cm$^{-3}$) LEC-GaAs wafers, with (100) surfaces and thicknesses $d\approx 0.5$ mm. Irradiations were performed at a Van de Graaff accelerator with 3 MeV electrons, using a current density of 8 $\mu$A/cm$^2$, while the samples were directly cooled by a stream of liquid He.[24] The irradiation dose and temperature were *in situ* monitored by measuring the electrical resistivity of a copper wire that was irradiated simultaneously. The samples were irradiated with doses $\phi t$, between 0.6 and $3.6\times 10^{19}$ $e^-$/cm$^2$, respectively (see Table I).

During the high dose irradiation of the x-ray samples, some instabilities of the accelerator lead to a spontaneous heating of the samples, therefore an annealing stage around 10 K found with two samples could not be reproduced with others. Therefore, we start the comparison of the samples at $T=20$ K. After irradiation, the samples were transferred to the measuring cryostat without intermediate warming. Isochronal annealing ($\Delta t=15$ min) at each temperature was performed within the He atmosphere of the cryostat below room temperature and under vacuum ($p\leqslant 10^{-5}$ Pa) at higher temperatures. Before irradiation, the samples had been annealed under the same conditions at the expected highest annealing temperature of 800 K.

### B. X-ray diffraction

The experimental methods used for the measurements of the diffuse scattering have been described earlier[25,26] and for the present investigation, we used Cu $K\alpha_1$ radiation from a 12 kW rotating anode tube and a germanium (111) monochromator. The lattice parameter was determined with a

TABLE I. Samples and irradiations.

| No. | Type | $\phi t$ ($10^{19}$ $e^-$/cm$^2$) | $\Delta a/a$ ($10^{-6}$) | $(\Delta a/a)/\phi t$ ($10^{-24}$ cm$^2$) | $S_n^{sym}q^2/k^2$ ($10^{-3}$ a.u.) (400) | (511) | (422) | (444) | $c\Pi^{(1)}/\phi t$ ($10^{-20}$ eV$^2$ cm$^2$) | $\Pi^{(2)}/\Pi^{(1)}$ | $\Pi^{(3)}/\Pi^{(1)}$ |
|---|---|---|---|---|---|---|---|---|---|---|---|
| 1 | s.i. | 0.60[a] | 65 | 10.8 | 1.9 | 1.8 | | | 2.1 | 0.027 | 0.084 |
| 2 | s.i. | 1.28[a] | 179 | 13.7 | 3.6 | 4.2 | | | 2.0 | 0.032 | 0.080 |
| 3 | s.i. | 1.76 | 202 | 11.5 | 6.2 | 6.4 | | 6.4 | 2.5 | 0.030 | 0.100 |
| 4 | s.i. | 2.32[a] | 317 | 13.6 | 6.7 | 7.9 | | | 2.2 | 0.035 | 0.085 |
| 5 | *n* | 0.61 | 81 | 13.3 | 3.2 | 3.7 | | | (3.8) | 0.040 | 0.100 |
| 6 | *n* | 1.72 | 213 | 12.4 | 6.6 | 6.9 | | 6.5 | 2.6 | 0.035 | 0.102 |
| 7 | *n* | 3.63[b] | 376 | 10.4 | 13.0 | 13.0 | 14.5 | | 2.5 | 0.038 | 0.095 |
| 8 | *p* | 0.61 | 64 | 10.5 | 2.9 | 2.4 | | | 2.9 | 0.025 | 0.105 |
| 9 | *p* | 1.27 | 127 | 10.0 | | 4.1 | 4.6 | | 2.3 | | |
| 10 | *p* | 1.72 | 180 | 10.4 | 5.8 | 5.8 | | | 2.3 | 0.030 | 0.108 |
| Average | | | | $11.6\pm0.5$ | | | | | $2.38\pm0.1$ | $0.032\pm0.002$ | $0.095\pm0.003$ |

[a]Dose has been recalibrated as compared to Ref. 16, using the damage rate for copper from Ref. 27.
[b]The irradiation was performed with 2.5-MeV electrons and the given dose is the expected value for 3-MeV electrons.

modified Bond technique,[28] using the asymmetric (711) reflection. Diffuse scattering was measured close to the (400) and (511) reflections and for some samples additionally at (422) and (444) reflections; an angular region of $\pm 6°$ was scanned in the $\vartheta - 2\vartheta$ mode, with a typical step width of 0.25°. By the use of a linear position sensitive detector, the two dimensional intensity distribution around the reflection was obtained in this way. Absolute intensities were obtained by calibration with a polystyrene standard (for details see Ref. 23). The defect induced scattering intensity was separated from the total scattering intensity observed after irradiation by subtraction of the background that was measured before irradiation and after total annealing of the samples. This background is mainly determined by the thermal diffuse scattering, the Compton scattering and some tails of the Bragg-Peak and can be assumed to be unaffected by the present concentrations of point defects.[29]

## IV. EXPERIMENTAL RESULTS

In this section, we first show the most characteristic features of the diffuse scattering intensity in some examples. After that, we show the changes of the HDS and of the lattice parameter as a function of the irradiation dose and the annealing temperature. The quantitative results are summarized in Table I which is discussed in the following Sec. V.

### A. Distribution of the HDS intensity

Figure 1 shows the irradiation induced increase of the diffuse scattering intensity close to a (511) reflection. The intensity is shown for a radial scan in reciprocal space (i.e., **q** parallel **G**) and is therefore essentially determined by $\Pi^{(1)}$ [Eq. (6) of Ref. 20]. After subtraction of the background the HDS scattering cross section, $S_H$ can be determined from these intensities. In order to allow for a direct comparison of the scattering cross section determined at different Bragg reflections considering the crystal anisotropy, all values of $S_H$ have been normalized by $\gamma^{(1)}$ [Eq. (6) of Ref. 20]:

$$S_n = S_H \frac{\gamma^{(1)}(100)}{\gamma^{(1)}}. \tag{3}$$

Hence, the scattering function has its original values for $(h00)$ type reflections and includes a correction for other reflection types.

Figure 2 shows $S_n$ close to a (511) reflection as a function of the distance **q** from a reciprocal lattice vector. Due to the multiplication of $S_n$ with $q^2$, we expect a horizontal line if the scattering law [Eq. (6) of Ref. 20] is exactly valid. Such a behavior seems to be valid after annealing of GaAs above 300 K, but there is a decrease of $S_n q^2$ for small values of $q$ after irradiation. In addition, we observe a large asymmetry of $S_n$ for negative and positive deviations from the Bragg

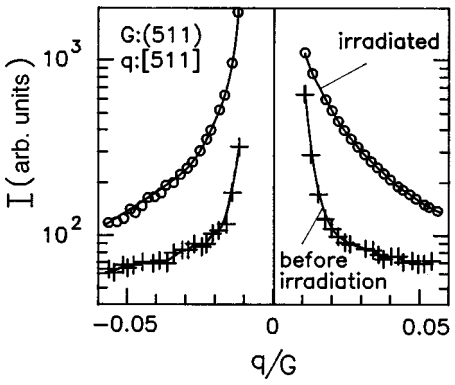


FIG. 1. Diffuse scattering intensity close to a (511) reflection in a [511] direction of **q**. The intensity observed after irradiation ($\phi t = 3.6\times10^{19}$ $e^-$/ cm$^2$ at 4.5 K, sample 7) is compared to the background measured before irradiation and after annealing at 770 K.

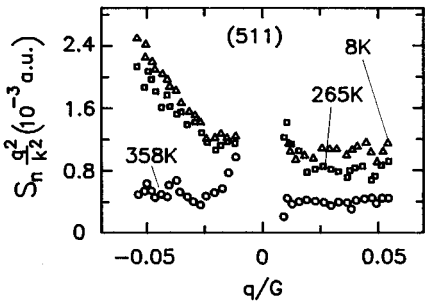


FIG. 2. Variation of the diffuse scattering cross section $S_n$ close to the (511) reflection of irradiated GaAs ($\phi t = 3.6 \times 10^{19}$ $e^-/\mathrm{cm}^2$, sample 7). The direction of **q** is parallel to the reciprocal lattice vector **G**. $S_n$ is given in units of the average atomic scattering factor and is shown as observed after irradiation (8 K) and after annealing at 265 K and 358 K.

peaks. For the (511) reflection, this asymmetry is not obvious in Fig. 1, as it is modified by the variation of the structure factor $F$. The symmetric part of the Huang scattering can directly be separated from this total scattering [Eq. (4) of Ref. 20] and is shown in Fig. 3. The separation of the antisymmetric scattering does not remove the deviations from the $q^{-2}$ behavior. The figure shows in addition that these deviations seem to scale with the value of $q$ at different Bragg reflections; such a behavior generally indicates defect correlations. The remaining antisymmetric scattering [Eq. (5) of Ref. 20] is shown in Fig. 4 after multiplication with $q$ as we expect a $q^{-1}$ law if this contribution is due to the interference of the Huang scattering amplitude with higher order terms. In contrast to the expectation for highly distorting defects we observe, however, a change of the sign of $S_n^{\mathrm{asy}}$ comparing different Bragg reflections. Hence, we observe all characteristic features of the diffuse scattering intensity from close FP's, as discussed in Sec. II.

From the intensity distribution around the Bragg peak, we can determine the symmetry parameters $\Pi^{(2)}$ and $\Pi^{(3)}$. Again, we have multiplied the intensity by $q^2$ and averaged

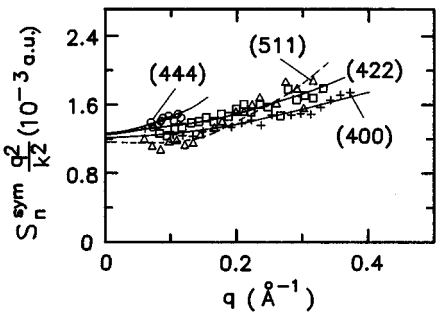


FIG. 3. Symmetric part of the HDS as observed at different Bragg reflections for sample 7 ($\phi t = 3.6 \times 10^{19}$ $e^-/\mathrm{cm}^2$; annealing temperature $T_a = 10$ K). The different lines present a polynomial fit to the data that is intended as a guide to the eye and shows, in addition, that a rather consistent value is obtained for the extrapolation to $q = 0$.

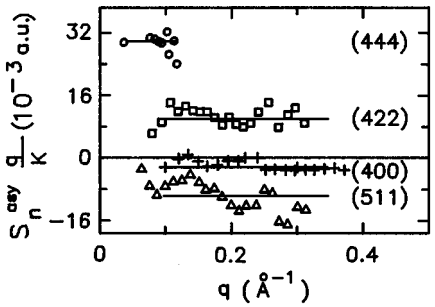


FIG. 4. Antisymmetric part of the HDS for the same sample as Fig. 3.

within a range of $q$ ($0.09 < 0.18$ Å); the resulting averages are plotted in Fig. 5, as a function of the angle $\phi$ between **q** and **G**. In contrast to the expectation for a cubic or tetragonal defect displacement field, we observe intensity close to $\phi = 90°$, which means $\Pi^{(3)} \neq 0$. The numerical fit of Eq. (6) of Ref. 20 to the data is shown in Fig. 5 for different assumed symmetries. The improvement of the fit for $\Pi^{(2)} \neq 0$ shows that this deviation is significant, too, i.e., the average defect has orthorhombic symmetry. The quantitative parameters are given in Table I and are independent of the irradiation dose. The values of these parameters that quantify the deviation from cubic symmetry are rather large, as can be seen by a comparison to the values expected for strongly anisotropic defects like dislocation loops, e.g., a loop with Burgers vectors $b = \langle 110 \rangle$ and a (110) habit plane yields $\Pi^{(2)}/\Pi^{(1)} = 0.015$ and $\Pi^{(3)}/\Pi^{(1)} = 0.14$. These large values indicate again the presence of close FP's and, in this case, the symmetry parameters reflect the spatial orientation of the pair rather than the symmetry of the individual point defect.

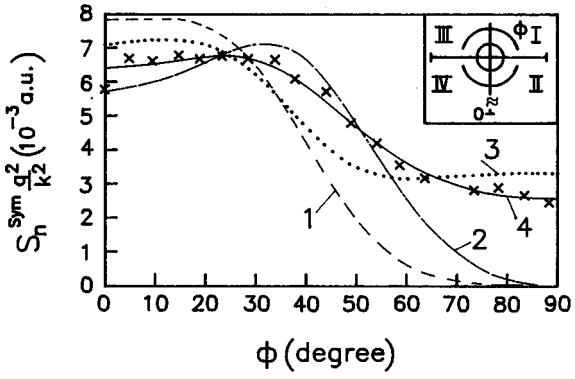


FIG. 5. Distribution of the scattering intensity around a (400) reflection. The intensities are averaged over a range of $q$ between 0.09 and 0.18 $\mathrm{Å}^{-1}$ and are plotted as a function of the angle $\phi$ between **q** and **G**. The data points present the average of the four quadrants shown in the inset. As the (400) direction presents a symmetry line of the crystal, the data from quadrant I and III as well as II and IV are equivalent; the additional averaging of I, II and III, IV selects the symmetric part of the scattering. Data taken after irradiation ($T_a = 10$ K) of sample 4: s.i. GaAs, irradiation dose $2.3 \times 10^{19}$ $e^-/\mathrm{cm}^2$. The different lines show fits assuming different defect symmetries: (1) cubic ($\Pi^{(2)} = \Pi^{(3)} = 0$), (2) tetragonal ($\Pi^{(3)} = 0$), (3) trigonal ($\Pi^{(2)} = 0$), and (4) orthorhombic ($\Pi^{(2)}$, $\Pi^{(3)} \neq 0$).

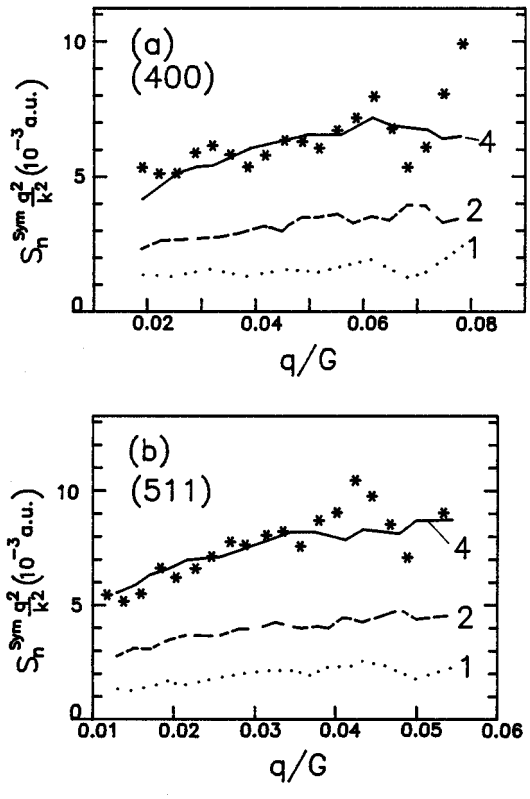


FIG. 6. Radial distributions of the symmetric part of the scattering intensity at (a) (400) reflections and (b) at (511) reflections observed after irradiation ($T_a=10$ K), of s.i. samples: 1: $\phi t=0.6\times10^{19}$ $e^-/\mathrm{cm}^2$; 2: $\phi t=1.28\times10^{19}$ $e^-/\mathrm{cm}^2$; and 4: $\phi t=2.3\times10^{19}$ $e^-/\mathrm{cm}^2$. The data are presented by the different lines and the lowest dose data (sample 1) are multiplied by the factor corresponding to the difference in dose as compared to sample 4 and plotted as additional points in order to demonstrate the independence of the distribution from the dose.

### B. Dose dependence

Figure 6 shows for the example of the (400) and (511) reflections of the s.i. samples that the typical structure of the scattering distribution, i.e., the deviation from a $q^{-2}$ behavior of $S_n$, is independent of the irradiation dose. Therefore, we can discuss the evolution of the average values over a larger region of $q$ with the irradiation dose. The values of $S_n$ are plotted in Fig. 7 and show a linear increase with the irradiation dose within an error limit of $\approx 10\%$. We observe no significant difference between doped and undoped samples (see also Table I). The linear increase of $S_n$, as well as of $\Delta a/a$, shows that stable defects must be produced continuously and that there are no doping atoms necessary to immobilize and stabilize the defects.

### C. Thermal annealing

Figure 8 shows the changes of the $q$ dependence of $S_n$ upon annealing, for a **q** direction parallel to **k** that mainly reflects the parameter $\Pi^{(1)}$ or $(V^{\mathrm{rel}})^2$. The decrease at small $q$ is no longer observed after annealing at 330 K. Hence, these deviations from the ideal HDS behavior seem to be characteristic for the FP's that anneal below RT.

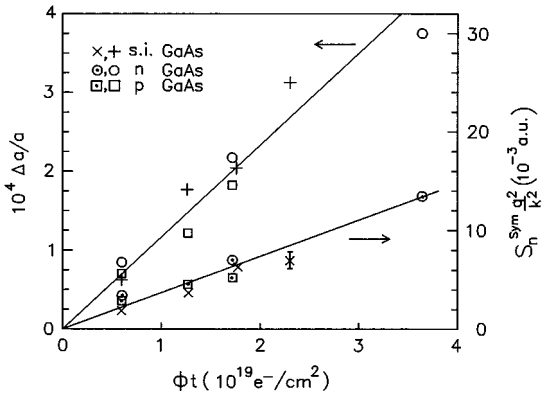


FIG. 7. Increase of the symmetrical part of the HDS cross section and of the lattice parameter as a function of the irradiation dose ($T_a=10$ K). The different symbols present different types of samples.

In contrast, we observe for $T_a \geqslant 330$ K a small increase of the intensity at small $q$. Such a behavior indicates the formation of defect agglomerates [Eq. (9) of Ref. 20]; however, the effect is small, i.e., only few or very small clusters or complexes may be present and the formation of larger agglomerates like dislocation loops during the defect migration at $T \geqslant 330$ K can be excluded. As the total scattering is always decreasing, we cannot decide at present whether the small clusters are already formed during irradiation or along with the defect reactions in the annealing stages I and II.

Figure 9(a) summarizes the annealing behavior of $S_H$ (again for $\mathbf{q}\|\mathbf{G}$) and Fig. 9(b) shows the annealing of $\Delta a/a$. HDS and $\Delta a/a$ show the dominant stage around RT

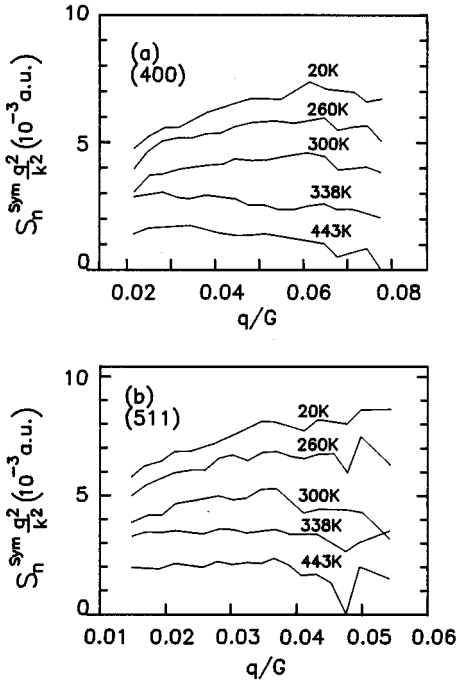


FIG. 8. Change of the radial distribution of the symmetric part of the HDS during annealing. (a) Close to the (400) reflection and (b) close to the (511) reflection of sample 4 (s.i., $\phi t=2.3\times10^{19}$ $e^-/\mathrm{cm}^2$).

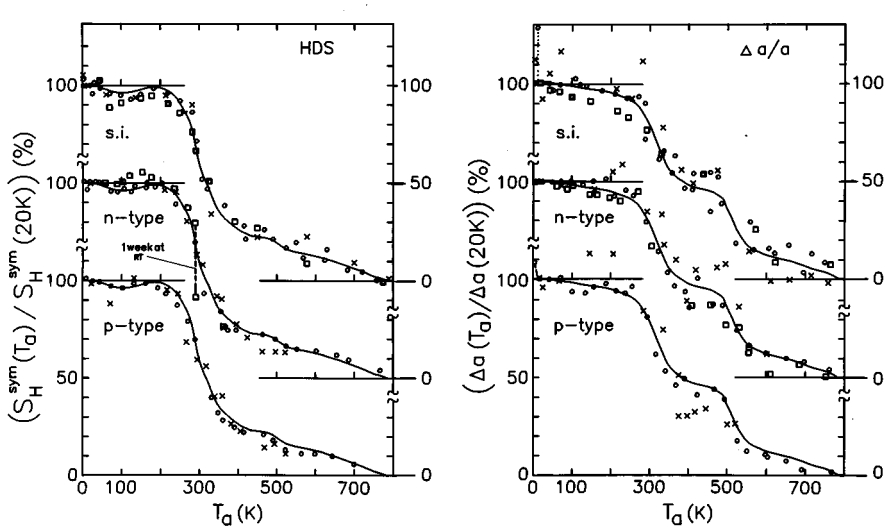


FIG. 9. Annealing behavior of the HDS intensity (a) and of the change of the lattice parameter (b) for s.i., *n*-type and *p*-type GaAs irradiated at 4.7 K. The irradiation doses are characterized by different symbols: ×: $0.6\times10^{19}$ $e^-/\mathrm{cm}^2$; ○: $(1.3-1.7)\times10^{19}$ $e^-/\mathrm{cm}^2$; and □: $(2.3-3.6)\times10^{19}$ $e^-/\mathrm{cm}^2$. In addition to the specified samples, the same average annealing curve obtained by neglecting the lowest dose irradiation is always shown for comparison. Data are normalized at $T_a=20$ K.

that is larger for $S_H$ than for $\Delta a/a$; in contrast, the 500 K stage is larger for $\Delta a/a$ than for $S_H$. Considering the larger error bars for the low dose irradiations, there is no systematic dose dependence observed. A possible dependence of the annealing on the doping should be revealed most clearly for the low irradiation doses, but $S_H$ shows again no relevant difference; only the annealing of $\Delta a/a$ seems to be faster for the *p*-doped sample that has also the highest doping level. Combining the values of $S_H$ and $\Delta a/a$ at the end of the RT stage [Eq. (14)] shows that the decrease of the relaxation volume of the average defects (as compared to the total average at 20 K) is about 20% smaller for this low dose irradiation of the Zn-doped sample than for the s.i. and *n*-type GaAs. Above the 500 K stage, there is within the errors no difference left. Except for these small differences at low irradiation doses, there is no major dose dependence or doping dependence in the annealing of $S_H$ and $\Delta a/a$, and we may consider only the average annealing behavior that is always shown as a reference line in Fig. 9.

With these average annealing curves, we can determine the relaxation volume of the defects remaining after annealing at $T_a$:

$$\frac{V^{\mathrm{rel}}(T_a)}{V^{\mathrm{rel}}(20\ \mathrm{K})}=\frac{S_H(T_a)\Delta a(20\ \mathrm{K})}{S_H(20\ \mathrm{K})\Delta a(T_a)}. \tag{4}$$

The corresponding defect concentrations remaining after annealing at $T_a$ are

$$\frac{c(T_a)}{c(20\ \mathrm{K})}=\frac{(\Delta a/a(T_a))^2}{(\Delta a/a(20\ \mathrm{K}))^2}\,\frac{S_H(20\ \mathrm{K})}{S_H(T_a)}. \tag{5}$$

Although there is only minor annealing within the region below 250 K, there is a reproducible decrease of $S_H$ of $\approx$ 10% already between 20 K and 100 K, which correlates with changes in the optical absorption.[16] Similar to the annealing in the main stage around RT, the lattice parameter changes less at these temperatures than $S_H$. Between 110 K and 250 K, we observe a minor increase of $S_H$ and combined with the slow and steady decrease of $\Delta a/a$, we deduce [Eq. (4)] a small increase of the average defect size that yields an increase of $\langle V^{\mathrm{rel}}\rangle$ by about 20% at the maximum of $S_H$ around 200 K; i.e., there are only small rearrangements and possibly only a part of the defects are involved.

The two major annealing stages around RT and 500 K are characterized by the different quantitative annealing of $S_H$ and $\Delta a/a$. The estimate of Eq. (4) yields that the low temperature defects are characterized by about twice as large relaxation volumes, $V^{\mathrm{rel}}$ (or displacement fields) as the defects remaining at 400 K. A major fraction of these smaller defects anneal around 500 K. At 600 K, the ratio of $S_H$ and $\Delta a/a$ approaches its original value, and there is complete annealing in a final stage between 600 K and 800 K.

The distribution of the diffuse scattering intensity around the different Bragg reflections does not change significantly during annealing: i.e., the ''apparent symmetry'' averaged over all defects remains orthorhombic, as shown by the variation of the symmetry parameters $\Pi^{(2)}$ and $\Pi^{(3)}$ in Fig. 10, that never approach a zero value. As indicated in the figure, the error bars of these normalized values increase at high temperatures along with the decrease of the total intensity, as shown in Fig. 9.

## V. DISCUSSION

### A. Changes of the lattice parameter

The quantitative results of the changes in lattice parameter and HDS are summarized in Table I. We observe a linear

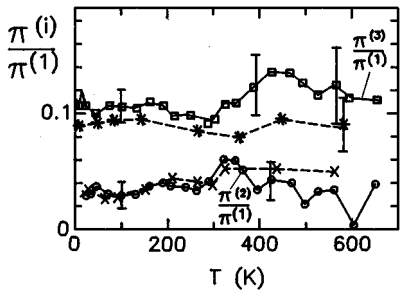


FIG. 10. Variation of the symmetry parameters $\Pi^{(2)}$ and $\Pi^{(3)}$, during isochronal annealing after low temperature electron irradiation. ×, * s.i. sample No. 4 and □, ○ *n*-type sample No. 7.

TABLE II. Relaxation volumes and introduction rates. Values of $V^{rel}$ and $\Sigma$ for the averages over all defects observed after irradiation and annealing at 20 K, 400 K (end of stage II), and 600 K (end of stage III). In addition, the values for the defects annealing between 20 K and 400 K [stage-(I,II) defects] and 400 K and 600 K (stage-III defects) are included.

| | Annealing temperature | | | Difference between annealing temperatures | |
|---|---|---|---|---|---|
| | 20 K | 400 K | 600 K | (20 K–400 K) stage-(I,II) defects | (400 K–600 K) stage-III defects |
| $\langle V^{rel}\rangle$ | $2.0\pm0.2$ | $1.0\pm0.2$ | $1.9\pm0.6$ | $2.9\pm0.4$ | $0.8\pm0.25$ |
| $\langle\Sigma\rangle$ | $0.8\pm0.1$ | $0.75\pm0.1$ | $0.09\pm0.03$ | $0.27\pm0.06$ | $0.67\pm0.25$ |

increase of the lattice parameter with the electron dose with no indication of a saturation behavior even after $\approx 3\times10^{19}$ $e^-/cm^3$. This yields an average increase of the lattice parameter of $\Delta a/a/\phi t=(1.16\pm0.1)10^{-23}$ per $(e^-/cm^2)$. This value can be compared with the results of length measurements on $n$-type GaAs that yield $(\Delta l/l)/\phi t=1.0\times10^{-23}$ $(e^-/cm^2)^{-1}$.[10] As these results have been obtained for 2-MeV electrons, we expect a 10%–25% increase of this value for 3-MeV electrons. The exact value of this increase depends on the assumptions on the role of double displacements and of the value of the threshold energy for the displacements.[30] Hence, there is very good agreement between the two experiments and we observe a linear increase over more than two orders of magnitude of the irradiation dose if we combine the data [$\phi t=2\times10^{17}-2\times10^{18}$ $e^-/cm^2$ (Ref. 10) and $6\times10^{18}-3\times10^{19}$ $e^-/cm^2$ for the present work]. The positive values of $\Delta a/a$ show that the absolute value of the relaxation volumes of the interstitial atoms (that is expected to be positive) is larger than that of the (presumably negative) $V^{rel}$ of vacancies. GaAs behaves, therefore, much different than InP or Ge, where the vanishing change of $\Delta a/a$ indicates a nearly complete cancellation of the displacement fields.[18]

### B. Evaluation of the diffuse scattering intensity

Before we can apply the HDS theory for a quantitative evaluation of $S_H$, the origin of the deviation from the $q^{-2}$ behavior must be discussed. A first assumption would be that the defects have a tendency for ordering. This ordering yields a decrease of $S_H$ at small $q$ as it is frequently observed in small angle scattering experiments at systems of higher concentration.[21,31] For this model we would, however, expect an increase of the effect with increasing irradiation dose. Although the dose range investigated is too small to exclude this effect definitely, there is no indication for a dose dependence in Fig. 7 or Table I. Thus, the correlation between the vacancy and the interstitial atom within the individual Frenkel pair and the corresponding modification of the displacement field seem to be the most appropriate explanation for the observation (Sec. II). This model explains simultaneously also the observed asymmetries of $S_H$ and shows that the average intensity over the accessible region of $q$ can be reasonably approximated by the HDS of the underlying individual defects. By the numerical fit of the three parameters $\Pi^{(1)}-\Pi^{(3)}$ to the distribution of this averaged intensity around different Bragg peaks [Eq. (6) of Ref. 20], we determined the value of $c\times\Pi^{(1)}$ that is given in Table I. This value is independent of the irradiation dose or the doping. The symmetry parameters $\Pi^{(2)}$ and $\Pi^{(3)}$ are normalized by $\Pi^{(1)}$ and show also no significant dependence on the irradiation dose or the doping. The errors of $\pm10\%$ for $c\times\Pi^{(1)}/\phi t$ arise from uncertainties in the irradiation dose (these might contribute differently to $S_H$ and $\Delta a/a$, due to inhomogeneities of the beam profile and corresponding strains in the sample), changes of the sample surface during irradiation that might affect special tails of the Bragg peak,[32] and from the counting statistics that affects especially the low dose. Within these errors, the results obtained close to different Bragg reflections agree quite well and, therefore, confirm the expected dependence of $S_H\sim G^2$ and the applicability of the HDS theory.

### C. Structure and concentration of the defects

Combining the average values for $\Delta a/a$ and $c\times\Pi^{(1)}$ we obtain, from Eq. (8) of Ref. 20, average values for $V^{rel}$ and the concentration $c$. In order to obtain a quantity that is independent of the actual irradiation dose, this concentration is expressed in terms of the introduction rate (or production rate) $\Sigma=c/(\Omega\phi t)$. These values are summarized in Table II, together with the values obtained from Eqs. (4,5) for the defects left after annealing at the end of stage II ($T_a\approx$ 400 K) and stage III ($T_a\approx$ 600 K). The value of $\langle V^{rel}\rangle$ (20 K) indicates rather large displacements and each defect increases the volume of the crystal by more than one atomic volume. For the highest irradiation dose, the observed introduction rate yields defect densities as high as $3\times10^{19}$ $cm^{-3}$. The defects remaining after RT annealing have a remarkably smaller $\langle V^{rel}\rangle$. The defects remaining at 600 K show again similar values as the original ones; hence, there is no indication for the formation of larger defect clusters during annealing.

The data of Table II are a nonlinear weighted average over all defects present in the sample and we need additional information for a separation. In a first step, we use the different annealing behavior (Fig. 9) of the defects to separate their contributions to $\Delta a/a$ and $S_H$; i.e., the defect annealing in stages I and II are characterized by $\Delta a/a=[\Delta a/a(20\text{ K})-\Delta a/a(400\text{ K})]$ and $S_H=[S_H(20\text{ K})-S_H(400\text{ K})]$. These data yield: $V^{rel}=(2.9\pm0.4)\ \Omega$ and $\Sigma=(0.27\pm0.06)\ cm^{-1}$. This procedure of separation is only valid as long as the annealing of $\Delta a/a$ and HDS is achieved by defect recombination and not by rearrangements; in order to check this, we have subdivided the annealing stage into smaller steps and

have obtained always similar results. Hence, the assumptions for these evaluations seem reasonably fulfilled.

These ''low temperature defects'' are characterized by much larger lattice distortions and smaller introduction rates than the remaining defects. The quantitative results of Table II can, however, not be simply deduced from a linear average of the individual defects, due to the quadratic dependence of $S_H$ on $V^{\mathrm{rel}}$. As PAS shows the dominant annealing of $V_{\mathrm{Ga}}$ related defects within this temperature range,[11–13] these defects are commonly attributed to the Ga sublattice. This attribution does not exclude that these FP's are part of a larger defect agglomerate and also include antisite defects[16] and we will call them more generally stage-(I, II) defects. As deduced from DLTS investigations,[7] the remaining defects should be dominated by FP's on the As sublattice, which anneal around 500 K or within stage III. In spite of the larger errors, which are connected with this smaller annealing stage, the results for the stage-III defects are characterized by a much smaller $V^{\mathrm{rel}}$. Within the errors, the results for these stage-III defects are the same as those for the total number of defects surviving at 400 K. There is no complete annealing at 600 K and the values of Table II indicate that a small fraction of all types of defects and small complexes might be surviving. This observation is in agreement with the observation of stable $V_{\mathrm{As}}$ by PAS,[13,33,34] as well as $V_{\mathrm{Ga}}$ by EPR (Refs. 35,36) up to this temperature.

For a quantitative discussion of the values given above, we must separate the contribution of the vacancies and interstitial atoms in addition and as long as there is no theoretical guide for the relative sizes of these defects, we discuss a range of parameters.

### *The stage-(I, II) defects*

As we have only the two equations [Eqs. (8) of Ref. 20] for the determination of $c$, $V_i^{\mathrm{rel}}$, and $V_v^{\mathrm{rel}}$ we may start the discussion of the values of $c$ or $\Sigma$ and $V_i^{\mathrm{rel}}$ by considering $V_v^{\mathrm{rel}}$ as a free parameter. For the simple assumption, $V_v^{\mathrm{rel}}=0$, the values given in Table II for the stage-(I,II) defects represent the interstitital atom and these values are specially marked in Fig. 11 which summarizes the possible solutions if we vary $V_v^{\mathrm{rel}}$. Due to the quadratic equation, there are generally two solutions for every given value of $V_v^{\mathrm{rel}}$. In the chosen presentation, all values for $V_i^{\mathrm{rel}}$ are lying on a circle and the shift of the center of the circle to positive values of $V_v^{\mathrm{rel}}$ reflects the experimental observation of a positive net change of $\Delta a/a$; the corresponding limiting value of $V_v^{\mathrm{rel}}$ for nonimaginary solutions is at $V_v^{\mathrm{rel}}\approx -0.6\ \Omega$. In the upper part of Fig. 11, the corresponding solutions for $\Sigma$ are shown in a logarithmic scale. From these mathematically compatible solutions, we can exclude a larger part by simple arguments.

(i) Equations (8) of Ref. 20 are symmetric in $V_i^{\mathrm{rel}}$ and $V_v^{\mathrm{rel}}$ and all solutions lying below the diameter starting at the zero point of the coordinate system simply present an interchange of $V_i^{\mathrm{rel}}$ and $V_v^{\mathrm{rel}}$ we expect quite generally that $V_i^{\mathrm{rel}}\geqslant V_v^{\mathrm{rel}}$ and will therefore concentrate the discussion on these solutions that are marked in Fig. 11 by the thicker semicircle. In order to facilitate the correct attribution of the corresponding solutions for $V_i^{\mathrm{rel}}$ and $\Sigma$, an additional dotted line is drawn along a part of the semicircle.

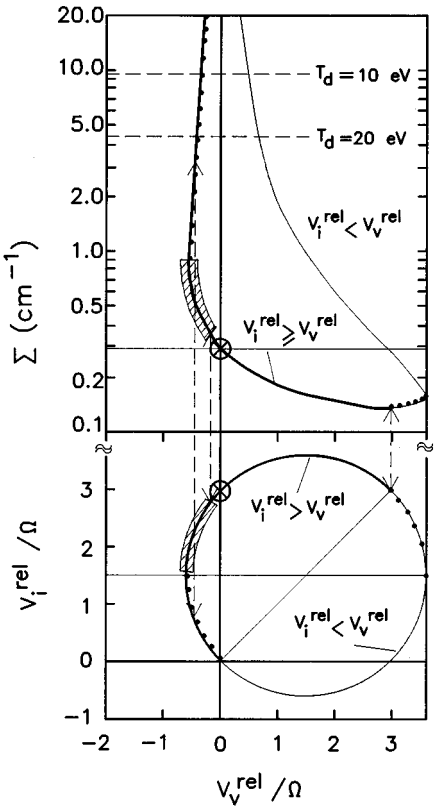


FIG. 11. Plot of the possible values of $V_i^{\mathrm{rel}}$ and $\Sigma$ for the stage (I,II) defects, using the relaxation volume of the vacancy $V_v^{\mathrm{rel}}$ as a parameter. The most probable region for the solution is indicated as a shaded area; for details see the text.

(ii) There is a band of solution along the dotted line that is connected with the diverging branch for $\Sigma$ and is not compatible with the threshold energy of $T_d\simeq 20$ eV observed for the stage-(I, II) defects;[7,8,13] this threshold energy allows a maximum value of $\Sigma\approx 4.4\mathrm{cm}^{-1}$ for 3-MeV electrons. This calculation assumes that every recoil with an energy above $T_d$ yields just one stable defect and allows for defect production on both sublattices; if defect production can start only from one sublattice, the expected maximum production rate would be lower by a factor of 2.

(iii) The FP model that is necessary for the explanation of the deviation from the $1/q^2$ law allows further discriminations. As we need opposite signs for $V^{\mathrm{rel}}$, due to interstitials and vacancies, this allows only for solutions with $V_v^{\mathrm{rel}}<0$. In spite of this restriction of the parameter, quite large differences for $V_i^{\mathrm{rel}}$ and $\Sigma$ are possible, considering that, for $V_v^{\mathrm{rel}}<-0.4\ \Omega$, both solutions are allowed: e.g., for $V_v^{\mathrm{rel}}=-0.5\ \Omega$ we obtain

$$V_i^{\mathrm{rel}}=2.0\ \Omega;\ \ \Sigma=0.5\ \mathrm{cm}^{-1}$$

as a first solution and

$$V_i^{\mathrm{rel}}=0.8\ \Omega;\ \ \Sigma=2.5\ \mathrm{cm}^{-1}$$

as a second solution.

Remarkably, the result for $V_i^{\mathrm{rel}}$ of this second solution is very similar to the values estimated above for the second type of defects. For a final distinction, we use the more specific details of the FP model. Hence, we combine the average

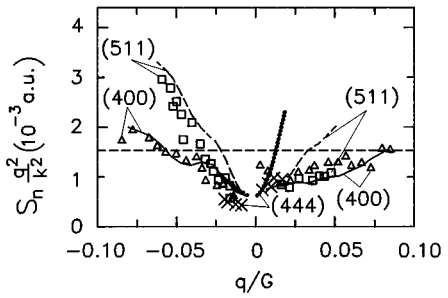


FIG. 12. Comparison of model calculations (lines) of the HDS from FP's in GaAs with the experimental results (data points) for the defects annealing around RT: $S^n$(20 K)–$S^n$(400 K). The model assumes $V_i^{\rm rel}=2.7\ \Omega$, $V_v^{\rm rel}=-0.7\ \Omega$, and a distance of the pair of $1.9a$ close to a [111] direction (the scattering of the equivalent defect orientations is averaged). The dashed horizontal line corresponds to the symmetric part of the scattering for randomly distributed vacancies and interstitial atoms and an introduction rate of $\Sigma=0.54\ {\rm cm}^{-1}$ was assumed in order to obtain a similar absolute value of the cross sections as for the experimental data. The experimental data represent sample No. 7 ($\phi t=3.6\times10^{19}\ e^-/{\rm cm}^2$).

values for $\langle S_H\rangle_q$ with the value deduced from the extrapolation of $S_H$ to $q\rightarrow0$, and obtain from Eq. (8) of Ref. 20 combined with Eq. (1) a direct value for the introduction rate: $\Sigma\approx0.6\ {\rm cm}^{-1}$. Although this extrapolation includes larger uncertainties and depends on the assumption that all defects show a similar scattering, this value should be precise enough to exclude the second branch of solutions with the small values for $V_i^{\rm rel}$ and the large values of $\Sigma$.

In addition, we performed detailed numerical simulations of the scattering from close FP's within the simple isotropic model, in order to reproduce the experimental details (deviation from the $1/q^2$ law, asymmetry, values of $\Pi^{(2)}$, $\Pi^{(3)}$). The result for FP's with a separation between vacancy and interstitial atom of $R_{\rm FP}=1.9$ a and $V_i^{\rm rel}=2.7\ \Omega$ and $V_v^{\rm rel}=-0.7\ \Omega$ is shown in Fig. 12 and compared to the experimental results for the stage-I, -II defects, i.e., $S_H$(20 K)–$S^H$(400 K). The distribution of $S_H$ is quite well reproduced. In addition, the model reproduces the large values of $\Pi^{(2)}$ and $\Pi^{(3)}$ (Table I) if the direction of $R_{\rm FP}$ is close to [111]. The fit of the absolute intensity yields an introduction rate $\Sigma=0.54\ {\rm cm}^{-1}$ for these pairs and the figure shows, in addition, that the symmetric part of the scattering of the corresponding uncorrelated defects agrees quite well with the average intensity over the experimentally accessible range of $q$ values as it was assumed above. Hence, these simulations also support the values deduced for branch 1, and considering larger uncertainties, the possible results should be within the range $V_v^{\rm rel}=-0.3\ \Omega$ and $-0.6\ \Omega$, that is indicated in Fig. 11. As $S^H(q\rightarrow0)$ indicates values of $V_v^{\rm rel}$ close to the limiting value, the most probable results are

$$V_v^{\rm rel}=-(0.55\pm0.1)\ \Omega,$$

$$V_i^{\rm rel}=(1.9\pm0.3)\ \Omega, \qquad (6)$$

$$\Sigma=(0.6\pm0.15)\ {\rm cm}^{-1}.$$

The errors of 10–20 % consider the variation of the experimental results (Table I) and allow for the additional uncertainty due to the separation of the stage-(I,II) defects from the total scattering. Although there is no indication for a deviation from the underlying assumption of a dominating contribution of similar close FP's, it should be kept in mind that such deviations [either due to defect clustering during annealing that yields a value too large for the subtracted $S$ (400 K), or due to a simultaneous annealing of uncorrelated FP's that yields a too high value for $S^{q\rightarrow0}$ (20 K)] would mean that the given results represent minimum values for $\Sigma$ and upper limits for $V_i^{\rm rel}$.

The observed production rate seems to be in good agreement with an estimate based on the combination of PAS results[12] with earlier results of measurements of the Hall effect[37] that yield a value of $\Sigma\approx0.46\ {\rm cm}^{-1}$ for 1.5 MeV electrons. The deduced production rate is, however, well below the maximum value expected for $T_d\approx20$ eV. As the threshold energy is investigated in GaAs only for two special crystallographic directions, the spacial average that is relevant for our irradiations with energies far above the threshold energy is not known. Considering the detailed investigations for metals,[27] this average displacement energy might be higher by a factor of 2 to 3 yielding correspondingly lower values of $\Sigma$. In addition, we might expect that during prolonged irradiation, a certain percentage of the close FP's recombines possibly supported by ionization induced jumps.[38,39] Hence, we cannot draw conclusions, e.g., on the involvement of only one sublattice, from this difference.

The value of $V_i^{\rm rel}\approx2\ \Omega$ is still rather large for a single interstitial atom in a rather open lattice. With our present knowledge about defects in semiconductors such a value cannot, however, be excluded considering, in addition, that rather large relaxation volumes have occasionally been observed for close packed crystals (e.g., Zn Ref. 26 or some alkali halides[40]). Nevertheless, it seems more reasonable to attribute this set of data to a larger complex, i.e., to the result of a double displacement that is consistent with the high threshold energy observed so far for the defects that anneal below RT.[8,13] Such a complex of two vacancies and two interstitial atoms would not change the evaluation of the HDS, however, the interpretation is modified as the values given above refer to the complexes and the total introduction rate of FP's would be twice as large, whereas the contribution of the single defects to the observed relaxation volumes would be half as large (i.e., $V_i^{\rm rel}\approx1\Omega$; $V_v^{\rm rel}\approx-0.3\ \Omega$, and $\Sigma_{\rm single}\approx1.2\ {\rm cm}^{-1}$; this value of $\Sigma_{\rm single}$ will, however, not be observed by most experiments, as they monitor only one signal of the total complex). The characteristic cancellation of the long range displacements can be achieved for such complexes in a similar way as for single FP's, however, the large number of additional free parameters does not allow us to prove or disprove one of these models by numerical similations based on the present data. There is a very recent indication for the production of FP's on the Ga sublattice, with the low threshold energy of $T_d=10$ eV,[41] which will be discussed in more detail in a forthcoming paper.[42] On the one hand, the observed room temperature annealing of some defects produced with $T_d\approx10$ eV indicates that the average parameters observed here contain also contributions of such

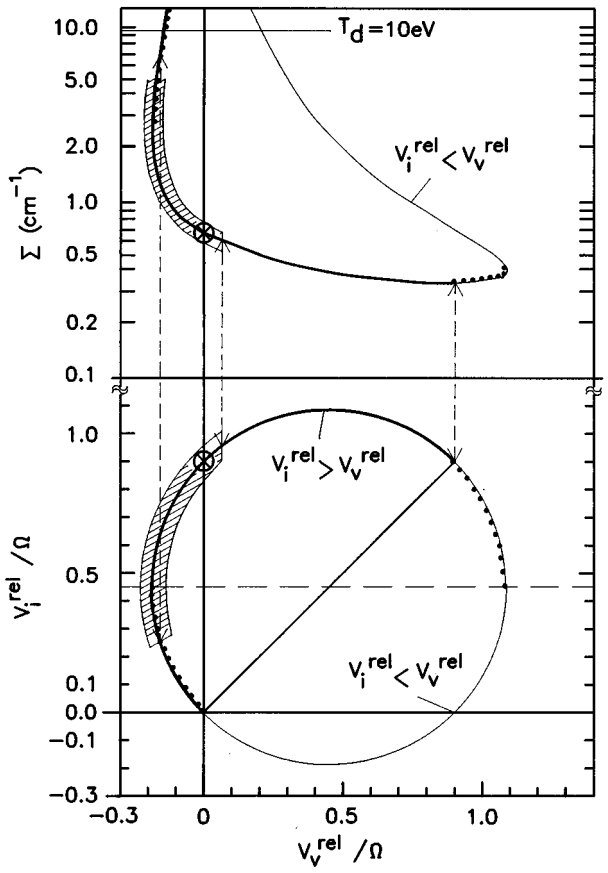


FIG. 13. Plot of the possible values of $V_i^{\mathrm{rel}}$ and $\Sigma$ for the stage III defects using the relaxation volume of the vacancy, $V_v^{\mathrm{rel}}$, as a parameter.

smaller defects. On the other hand, the observation of these defects gives strong support to the attribution of the ''20-eV defects,'' which seem to dominate the HDS, as well as the PAS (Ref. 13) to double displacements. With this attribution, we obtain quite similar characteristics for the FP's on both sublattices and these values are also of the same order of magnitude as those for InP ($V_i^{\mathrm{rel}}=-V_v^{\mathrm{rel}}=0.5\ \Omega$–$1.0\ \Omega$).[20]

### *The stage-III defects*

After annealing at RT, we observe a nearly perfect $q^{-2}$ behavior of the scattering intensity (Figs. 2,8); there is only a small increase of $S\times q^2$ at the smallest $q$ values, which might indicate the contribution of some smaller agglomerates. These deviations change the average value of $\langle S\times q^2\rangle$ by less the 10% and can be neglected in a first approximation. The average values of $\langle V^{\mathrm{rel}}\rangle$ and $\langle\Sigma\rangle$ obtained for all defects remaining after annealing at 400 K and for the defects annealing between 400 K and 600 K are very similar (Table II). Therefore, we start with an average value of $V^{\mathrm{rel}}\approx 0.9$ and $\Sigma\approx 0.7$ for these stage-III defects. Figure 13 shows the dependence of the results on the assumption on $V_v^{\mathrm{rel}}$ in a similar way as Fig. 11 did for the stage-(I,II) defects. For this smaller starting value, we obtain a much smaller negative limiting value for $V_v^{\mathrm{rel}}\approx -0.17\ \Omega$. As there is no additional information from the deviation of the ''ideal HDS'' behavior, we cannot *a priori* exclude small positive $V_v^{\mathrm{rel}}$ values for these defects. But a certain range of solutions can be excluded again as it is connected with values of $\Sigma$ larger than $9.5\ \mathrm{cm}^{-1}$, i.e., the expected maximum value for $T_d=10$ eV. Although we are left with a large range of possible solutions, the most plausible solutions should be on the side of negative $V_v^{\mathrm{rel}}$ and larger values for $V_i^{\mathrm{rel}}$, i.e.,

$$V_{\mathrm{rel}}^{v}=(-0.08\pm 0.08)\ \Omega,$$

$$V_i^{\mathrm{rel}}=(0.8^{+0.1}_{-0.3})\ \Omega, \tag{7}$$

$$\Sigma=(\ 0.9\ ^{+1.1}_{-0.2}\ )\ \mathrm{cm}^{-1}.$$

Again, the production rate is much below the maximum value expected for $T_d\approx 10$ eV and it is also lower than the DLTS results[7] that were obtained at very low irradiation doses ($\Sigma=1.5\ \mathrm{cm}^{-1}$ at 1 MeV corresponding to $\Sigma\approx 2\ \mathrm{cm}^{-1}$ at 3 MeV). As these DLTS levels were attributed to close FP's on the As sublattice, this value is a minimum value for the total damage and the difference to our results must be explained by irradiation induced recombination (as discussed for the stage-I, II defects), such that less than 50% of the directly produced defects form stable defects.

It seems remarkable, in addition, that the x-ray investigations showed the presence of a large number of close FP's for the stage (I,II) defects and did not show the characteristics of close FP's for the As sublattice, where these close pairs have been postulated since the early DLTS investigations.[2,7] Within the given data set, this difference could be easily explained by the small displacements for vacancies that have no observable effect on the displacement field of the interstitial atom. There might also be some small defect agglomerates that compensate for a decrease of $Sq^2$ at small $q$; this superposition seems, however, not to be the main contribution, as we observe no difference in the distribution of $Sq^2$ for the total intensity at $T_a=400$ K and the differential annealing $[S(400\ \mathrm{K})-S(600\ \mathrm{K})]$.

We cannot definitely exclude the solutions of the second branch lying around $V_v^{\mathrm{rel}}\approx -0.15\ \Omega$; $V_i^{\mathrm{rel}}=0.25\ \Omega$, $\Sigma=5\ \mathrm{cm}^{-1}$. This solution drastically increases the production rate up to values not far from the theoretical limit. In this case, we have a very small displacement field around the interstitial atom, and we might speculate about the correlation of this small size to the presence of this defect within the EL2 complex. For this case, the compensation of the displacement field of close FP's should, however, be very pronounced and the missing observation of this effect could only be due to a too large FP separation or to the superposition of clusters.

Hence, besides the much smaller average size of the stage-III defects [Eq. (7)], as compared to the stage-(I,II) defects [Eq. (6)], there remain open questions about the details. Theoretical calculations of displacements around vacancies and interstitial atoms might be of great help in the final selection between the different solutions, which are compatible with the experiment. In addition, the displacement fields around antisites might be important, as recent simulations indicate that antisites are produced very effectively by low energy replacement collisions.[43]

### D. Defect reactions

#### *Defect reactions during irradiation*

We observed a linear increase of $\Delta a$, as well as $S_H$ (Fig. 7 and Table I) up to an irradiation dose of $3\times10^{19}$ $e^-/\mathrm{cm}^2$. Taking a total introduction rate of $\Sigma\approx1\,\mathrm{cm}^{-1}$, this dose corresponds to defect densities of $3\times10^{19}$ $\mathrm{cm}^3$ or concentrations of $0.7\times10^{-3}$. There is neither an indication of a saturation behavior within the investigated dose range, nor an indication of defect clustering; in addition, there is no indication of a major influence of the doping. These observations can be directly understood if, independent of the production by single or double displacements, the FP's are immediately frozen in at the irradiation temperature of 4 K. As the FP's [at least the stage-(I,II) defects] seem to be stable within a rather small separation distance of $R_{\mathrm{FP}}\approx9$ Å, high concentrations can be achieved, and it seems plausible that no saturation is observed, since the highest defect concentration approached here corresponds to an average defect separation $d\simeq65$ Å ($d\simeq1/\sqrt[3]{N_d}$).

This static picture seems to be at variance to the possible ionization induced mobility of the interstitial atoms. Recombination enhanced defect mobility has first been observed in GaAs by DLTS measurements[37] and the dependence of the efficiency of these processes on the doping have been discussed.[38] Direct evidence for the interstitial mobility was obtained from the observation of the interaction of $\mathrm{As}_i$ with $B$ atoms, during 130 K irradiations.[44] In order to combine all these observations, we have to assume that mobile $\mathrm{As}_i$ are trapped at low doses at some impurities and as soon as the impurities are occupied, these traps are saturated and do not attract further $\mathrm{As}_i$, probably due to Coulomb repulsion. The only remaining possible traps are other vacancies, antisites, or vacancy antisite complexes that are continously produced along with the interstitial atoms;[18] hence, we form again many close FP's during prolonged irradiation. The possible mobility of the $\mathrm{Ga}_i$ has, for a long time, been assumed to lead to the immediate recombination of the "Ga FP's";[7,2] however, we have evidence for surviving Ga FP's from optical absorption spectroscopy[41,42] and we might, therefore, assume similar reactions on both sublattices. In addition to the double displacements, this mobility might contribute to the formation of the "large" stage-(I,II) defect discussed above. Very similar mechanisms for the evolution of the defect pattern seem to operate in InP.[20]

#### *Defect reactions during thermal annealing*

The annealing of $\Delta a/a$ and $S_H$ has been summarized in Fig. 9 and shows a steady background annealing and dominant annealing stages around RT (corresponding to Thommens stages I and II), around 500 K (stage III), and final annealing within a broad stage between 600 K and 800 K. The dominance of the RT stage is in agreement with the results of other macroscopic methods, i.e., measurements of the length change[10] and of the thermal conductivity.[9] The difference compared to DLTS results reveals that spectroscopic methods might miss a large fraction of defects.

The interpretation of the annealing reactions can follow the established lines:[2,7] the RT stage is dominated by the recombination of Ga FP's as PAS shows the disappearing of Ga vacancies,[11–13] and stage III is attributed to the annealing of arsenic FP's. Both annealing stages seem to be initiated by the detrapping and migration of the interstitial atoms, $\mathrm{Ga}_i$ and $\mathrm{As}_i$, respectively, as there are indications for the stability of the single vacancies [$V_{\mathrm{As}}$ (Refs. 2,13,33,34), $V_{\mathrm{Ga}}$ (Refs. 35,36)] up to the final stage between 600 K and 800 K. In further agreement with the observation of vacancy clustering[45] and with the independently determined migration energy of $V_{\mathrm{Ga}}$,[46] this final annealing can be attributed to the mobility of vacancies.

The most remarkable result of the HDS is the observation that this interstitial mobility leads (essentially) only to the recombination of FP's and not to the formation of larger complexes. Hence, the defect reactions below 600 K are very similar to those observed during irradiation: the annealing reactions seem to be dominated by local FP recombination and, especially for the RT stage, by subsequent rearrangements of the defect arrangement of the double displacements; the effects of long range migration are much suppressed by the saturation of the possible traps due to Coulomb repulsion. As the defect concentrations are much higher than the concentration of the doping atoms, there is no major influence of the doping. Hence, as a general observation, that is very similar also to InP,[20] there is no tendency towards the formation of larger agglomerates of like atoms neither during low temperature irradiation nor during subsequent annealing. In contrast to that, perfect interstitial loops have been observed to grow during irradiation at higher temperatures in the high voltage electron microscope.[47,48] This different behavior can be understood as loops are growing only at temperatures ($T\gg250\,^\circ\mathrm{C}$) where both types of interstitials are mobile: Under these conditions, electrically neutral agglomerates can grow by absorbing, in turn, defects with different charge.

## VI. SUMMARY AND CONCLUSION

X-ray-diffraction methods were used for a systematic investigation of the defects produced during low temperature electron irradiations of GaAs and of the defect reactions occuring during thermal annealing up to 800 K.

We observed a linear increase of the lattice parameter and of the intensity of the Huang diffuse scattering for irradiation doses ranging from 0.6 to $3.6\times10^{19}$ $e^-/\mathrm{cm}^2$. These results show that densities of FP's of at least $3\times10^{19}\mathrm{cm}^{-3}$ can be frozen in at low temperatures without indication of saturation. Specifically, the HDS excludes a continuous agglomeration and cluster growth of interstitial atoms during irradiation. Hence, the long lasting problem of the invisibility of the interstitial atoms[7] cannot be explained by the precipitation and/or loop formation at special traps. We rather present a model that explains the continous production of FP's by trapping and detrapping reactions of mobile interstitial atoms at vacancies and/or antisite atoms. These complexes cannot grow further, due to the Coulomb repulsion of additional interstitials. Consistent with this intrinsic defect stabilization, we did not observe a significant difference in the defect production between s.i. GaAs, $n$-type GaAs (Te), and $p$-type GaAs (Zn).

Due to the different annealing behavior, we were able to identify two different types of Frenkel defects. The first type anneals within the dominating annealing stage around room

temperature. It is characterized by large lattice relaxations and the superposition of positive displacements of interstitials with the negative displacements of vacancies. These pairs have a typical separation distance of $\approx 2$ lattice constants in a direction close to $\langle 111 \rangle$. A quantitative description in terms of the relaxation volumes yields: $V_i^{\mathrm{rel}} \approx 2\ \Omega$, $V_v^{\mathrm{rel}} \approx -0.55\ \Omega$; the production rate is $\Sigma = 0.6\ \mathrm{cm}^{-1}$ for these defects. The second type of Frenkel defects anneals within the 500 K annealing stage and is characterized by much smaller displacements or relaxation volumes: $V_i^{\mathrm{rel}} \approx 0.8\ \Omega$, $V_v^{\mathrm{rel}} = -0.1\ \Omega$, and an introduction rate of $\Sigma \approx 0.9\ \mathrm{cm}^{-1}$. The XRD results do not allow an attribution of the different Frenkel defects to different sublattices, and the recent observation of the simultaneous production of antisites[41–43] excludes such a strict separation, in principle. Nevertheless, the correlation of the results with PAS and DLTS investigations yields that $V_{\mathrm{Ga}}$ is a major constituent of the first type of defect and the FP's of the arsenic sublattice might dominate the second type. The large difference of the relaxation volumes leads (in combination with the different threshold energies for defect production[7,8]) to the conclusion that the larger defects represent complexes that result from double displacements. Assuming two FP's to be within such a complex, we obtain very similar relaxation volumes for all observed FP's in GaAs.

Final annealing is observed within a broad stage between 600 K and 800 K and can be explained by thermally activated vacancy migration. There is no indication for the growth of larger defect clusters during annealing and no significant influence of the doping. These observations can be explained in analogy to the defect reactions observed during irradiation.

Although there are some differences in the relaxation volumes, the defect production as well as the annealing behavior in GaAs is very similar to InP.[20] Hence, we may conclude that some general trends are emerging for Frenkel defects in III-V compounds and possibly also in other semiconductors.

## ACKNOWLEDGMENTS

The authors would like to thank Professor W. Schilling for his continuous support of this work and for many stimulating discussions. They are very grateful to Dr. Dworschak and the operating team of the Van de Graaff and to H.-J. Koslowski for technical assistance.

*Present address: Jena Optronic GmbH, Prüssing-Strasse 41, D-07745 Jena, Germany.

[1] M.O. Manasreh, D.W. Fischer, and W.C. Mitchell, Phys. Status Solidi B **154**, 11 (1989).

[2] J.C. Bourgoin, H.J.v. Bardeleben, and D. Stiévenard, J. Appl. Phys. **64**, R65 (1988).

[3] M. Kaminska and E.R. Weber, in *Imperfections in III-V Materials*, edited by E. R. Weber, Semiconductors and Semimetals Vol. 38 (Academic, New York, 1993) p. 59.

[4] G.A. Baraff, Acta Phys. Pol. A **82**, 599 (1992).

[5] J. Dabroswki and M. Scheffler, Phys. Rev. Lett. **60**, 2183 (1988).

[6] J.-M. Spaeth, M. Fockele, and K. Krambrock, Mater. Sci. Eng. B **13**, 261 (1992).

[7] D. Pons and J.C. Bourgoin, J. Phys. C **18**, 3839 (1985).

[8] K. Thommen, Radiat. Eff. **2**, 201 (1970).

[9] F.L. Vook, Phys. Rev. **135**, A1742 (1964).

[10] F.L. Vook, J. Phys. Soc. Jpn. **18**, 190 (1963), Suppl. II.

[11] C. Corbel, F. Pierre, P. Hautojärvi, K. Saarinen, P. Moser, Phys. Rev. B **41**, 10 632 (1990).

[12] C. Corbel, F. Pierre, K. Saarinen, P. Hautojärvi, and P. Moser, Phys. Rev. B **45**, 3386 (1992).

[13] R. Würschum, W. Bauer, K. Maier, A. Seeger, and H.-E. Schaefer, J. Phys. Condens. Matter **1**, 33 (1989), Suppl. A.

[14] D.W. Palmer, in *Radiation Effects in Semiconductors*, edited by N. B. Urli and J. W. Corbett, IOP Conf. Proc. No. 31 (Institute of Physics, London, 1977), p. 144.

[15] J.C. Bourgoin, Radiat. Eff. Defect Solids **111/112**, 29 (1989).

[16] A. Pillukat and P. Ehrhart, Mater. Sci. Forum. **83/87**, 947 (1992).

[17] K. Karsten and P. Ehrhart, Mater. Sci. Forum. **143/147**, 365 (1994).

[18] P. Ehrhart, K. Karsten, and A. Pillukat, in *Beam-Solid Interactions: Fundamentals and Applications*, edited by M.A. Nastasi, L.R. Harriott, N. Herbots, and R.S. Averback, MRS Symposia Proceedings No. 279 (Materials Research Society, Pittsburgh, 1993), p. 75.

[19] P.H. Dederichs, J. Phys. F **3**, 471 (1973).

[20] K. Karsten and P. Ehrhart, Phys. Rev. B **51**, 10 508 (1995).

[21] M.A. Krivoglaz, *Theory of X-Ray and Thermal Neutral Scattering by Real Crystals* (Plenum, New York, 1969).

[22] R. Coates and E.W.J. Mitchell, Adv. Phys. **24**, 593 (1975).

[23] K. Karsten, Report Forschungszentrum Jülich No. JÜL-2795, 1993.

[24] J. Hemmerich, W. Sassin, and W. Schilling, Z. Phys. **29**, 1 (1970).

[25] P. Ehrhart, in *Advanced Photon and Particle Techniques for the Characterization of Defects in Solids*, edited by J.B. Roberto, R.W. Carpenter, and M.C. Wittels, MRS Symposia Proceedings No. 41 (Materials Research Society, Pittsburgh, 1985), p. 13.

[26] P. Ehrhart, J. Nucl. Mater. **216**, 170 (1994).

[27] P. Jung, in *Atomic Defects in Metals*, edited by H. Ullmaier, Landolt-Börnstein, New Series, Group III, Vol. 25, Pt. 1 (Springer-Verlag, Berlin, 1991).

[28] W.L. Bond, Acta Crystallogr. **13**, 814 (1960).

[29] P. Ehrhart and W. Schilling, Phys. Rev. B **8**, 2604 (1973).

[30] O.S. Oen (unpublished).

[31] A. Guinier and G. Fournet, *Small Angle Scattering of X-Rays* (Wiley, New York, 1955).

[32] P. Ehrhart and U. Schlagheck, J. Phys. F **4**, 1589 (1974).

[33] M. Stucky, C. Corbel, B. Geffroy, P. Moser, and P. Hautojärvi, Mater. Sci. Forum. **10–12**, 265 (1986).

[34] C. Corbel, M. Stucky, P. Hautojärvi, K. Saarinen, and P. Moser, Phys. Rev. B **38**, 8192 (1988).

[35] A. Goltzené, B. Meyer, and C. Schwab, J. Appl. Phys. **57**, 1332 (1985).

[36] A. Goltzené, C. Schwab, J.P. David, and A. Roizes, Appl. Phys. Lett. **49**, 862 (1986).

[37] D.C. Look and I.R. Sizlove, J. Appl. Phys. **62**, 3660 (1987).

[38] D.V. Lang and L.C. Kimerling, Phys. Rev. Lett. **33**, 489 (1974).

[39] D. Stiévenard, X. Boddaert, J.C. Bourgoin, and H.J.v. Bardeleben, Phys. Rev. B **41**, 5271 (1990).

[40] H. Peisl, in *Defects and their Structure in Nonmetallic Solids*, edited by B. Henderson and A.E. Hughes (Plenum, New York, 1976), p. 381.

[41] H. Hausmann and P. Ehrhart, Mater. Sci. Forum. **196/201**, 1255 (1995).
[42] H. Hausmann and P. Ehrhart (unpublished).
[43] T. Mattila and R.M. Nieminen, Phys. Rev. Lett. **74**, 2721 (1995).
[44] R.C. Newman, J. Electron. Mater. **14A**, 87 (1985).
[45] Y. Itoh and H. Murakami, Appl. Phys. A **58**, 59 (1994).
[46] J.L. Rouviere, Y. Kim, J. Cunningham, J.A. Rentschler, A. Bourret, and A. Ourmazd, Phys. Rev. Lett. **68**, 2798 (1992).
[47] F. Reynaud and B. Legros-de Mauduit, Radiat. Eff. **88**, 1 (1986).
[48] D. Loretto and M.H. Loretto, Philos. Mag. A **60**, 597 (1989).